Limited accuracy of linearized gravity

John T. Giblin, Jr.,[1,2,*] James B. Mertens,[3,4,5,†] Glenn D. Starkman,[2,‡] and Chi Tian[2,§]

[1]*Department of Physics, Kenyon College, 201 North College Rd, Gambier, Ohio 43022, USA*
[2]*CERCA/ISO, Department of Physics, Case Western Reserve University, 10900 Euclid Avenue, Cleveland, Ohio 44106, USA*
[3]*Department of Physics and Astronomy, York University, Toronto, Ontario M3J 1P3, Canada*
[4]*Perimeter Institute for Theoretical Physics, Waterloo, Ontario N2L 2Y5, Canada*
[5]*Canadian Institute for Theoretical Astrophysics, University of Toronto, Toronto, Ontario M5H 3H8, Canada*

(Received 15 November 2018; published 28 January 2019)

Standard cosmological models rely on an approximate treatment of gravity, utilizing solutions of the linearized Einstein equations as well as physical approximations. In an era of precision cosmology, we should ask: are these approximate predictions sufficiently accurate for comparison to observations, and can we draw meaningful conclusions about properties of our Universe from them? In this work we examine the accuracy of linearized gravity in the presence of collisionless matter and a cosmological constant utilizing fully general relativistic simulations. We observe the gauge dependence of corrections to linear theory, and note the amplitude of these corrections. For perturbations whose amplitudes are in line with expectations from the standard Λ cold dark matter model, we find that the full, general relativistic metric is well described by linear theory in Newtonian and harmonic gauges, while the metric in comoving-synchronous gauge is not. For the most extreme observed structures in our Universe, such as supervoids, our results suggest that corrections to linear gravitational theory can reach or surpass the percent level in all gauges.

DOI: 10.1103/PhysRevD.99.023527

I. INTRODUCTION

It has been demonstrated that our Universe is mostly well described on large scales by a standard cosmological model, consisting of matter with properties similar to that of a pressureless perfect fluid and dark energy with properties similar to that of a cosmological constant [Λ cold dark matter (ΛCDM)]. At the same time, structures are formed through nonlinear interactions on scales only somewhat smaller than the Hubble scale—the Universe is decidedly inhomogeneous. These nonlinear interactions are commonly modeled using Newtonian N-body simulations, which account for nonlinearities in the matter sector, while large-scale inhomogeneities are commonly modeled using linear cosmological perturbation theory.

Such approximate treatments of gravitational interactions help improve the tractability of calculations, and offer us physical insight into the dominant gravitational effects. However, the connection between such approximate treatments and fully relativistic treatments is not often made nor fully quantified. Yet it is necessary in order to meaningfully interpret and understand theoretical predictions, especially given a goal of testing general relativity and alternatives to it in a cosmological setting. One concern is that, upon coarse graining a spacetime, we lose insight into the underlying properties of the spacetime. For example, this idea is at the core of the Ricci-Weyl problem [1], which has been shown to have implications for how observables are interpreted in an inhomogeneous universe [2]. Studies of nonlinear gravitational effects have also shown that energy from small-scale gravitational interactions can have a considerable impact on the cosmological properties of a spacetime [3,4]. Even within a standard perturbative cosmological framework, it has been shown that neglected relativistic effects can lead to percent-level or larger corrections when computing observables [5–7], providing a means by which we can study general relativity beyond its dominant behavior.

Numerical relativity offers us a unified framework in which to examine such questions, providing infrastructure largely agnostic to gauge and matter content, which, by construction, will exactly account for all gravitational effects. While the magnitude of effects on both observables and the spacetime metric have been examined in a standard cosmological setting using a fully relativistic approach [8–14], a more systematic examination of the order of magnitude of corrections to standard linear calculations has not yet been made. To this end, we compare linear theory to

*giblinj@kenyon.edu
†mertens@yorku.ca
‡glenn.starkman@case.edu
§cxt282@case.edu

fully general relativistic simulations performed without reliance on a background model or any perturbative assumptions. We evolve a collisionless stress-energy source and cosmological constant, with energy densities corresponding to values inferred from observations. We then explicitly demonstrate the gauge dependence of the magnitude of corrections to linear theory, and note the approximate order of magnitude in several commonly used gauges as a function of scale. We examine both overdensity amplitudes predicted by the ΛCDM model, as well as larger density contrasts consistent with observed structures.

We then examine in detail two measures of the inaccuracy of linear theory: we first compute the level of violation of the linearized Einstein field equations, and second compute the magnitude of disagreement of background Friedmann-Lemaître-Robertson-Walker (FLRW) quantities with spatially averaged quantities. The first of these measures provides us with a way to test the accuracy of linear gravitational theory. In linear theory, fields are often transformed between gauges using linearized definitions of gauge transformations; thus, a solution obtained in one gauge can be mapped to another gauge. Precise field values are then expected to differ between gauges, but in any gauge, corrections to linear gravitational theory should be of order $\mathcal{O}(h^2)$ for a metric perturbation amplitude h [15]. On the other hand, the average behavior of spacetimes is generally expected to agree with a FLRW model; thus, we directly compare the average properties of our simulations to a FLRW model. We observe the gauge dependence of this, and quantify the difference we observe across a range of physical scales.

When simulating density perturbations of statistically common amplitudes, we find that in comoving-synchronous gauge, the difference between fully relativistic and linear models of overdensities can be much larger than Newtonian and harmonic gauges, where the difference can be extremely small. For some of the largest structures in our Universe that have been observationally well characterized, we find that nonlinear effects can approach the percent level even in harmonic and Newtonian gauges, while linear theory is entirely unable describe the synchronous gauge metric. These findings coincide with expectations: it is well known that the amplitude of metric perturbations can vary significantly between gauges or "slicing conditions" [16], as noted in other approximate and analytic treatments [17,18] as well. For density perturbations of cosmologically common amplitudes in synchronous gauge, the metric amplitude scales roughly with the density contrast δ_ρ, and can therefore become quite large, while in harmonic slicing and a quasi-Newtonian gauge, metric perturbations remain small. The amplitude of metric perturbations in the presence of extreme structures, on the other hand, can be considerably larger than expected.

We begin in Sec. II by discussing the various methods we employ in order to obtain our results. In Sec. II A we briefly discuss the numerical relativity formulation we use to evolve Einstein's equations. In Sec. II B we discuss the formalism we use to evolve collisionless matter and some numerical details. In Sec. II C we describe the initial conditions we use in order to maintain consistency with standard cosmological calculations, and in Sec. II D we provide some discussion of the different gauges we use. We conclude by detailing our results in Sec. III, first describing the behavior of nonlinear corrections for various "mode-in-a-box" simulations with matter overdensity amplitudes predicted by standard cosmological perturbation theory, and finally performing asymmetric, fully 3-dimensional runs with observationally motivated physical parameters comparable to large voids and overdensities.

II. METHODS

Standard cosmology and numerical relativity employ similar, and sometimes coincident, formulations in which to study the behavior of Einstein's equations. Common to both is the $3+1$ language, in which the evolution of the spacetime metric is posed as a Cauchy problem, with spatial hypersurfaces evolved forward in time. We will generally remain within this framework, although will connect to both standard cosmological perturbation theory, which deals with the linearized Einstein equations, and formulations of numerical relativity, which are closely related to the $3+1$ decomposition.

A. Metric evolution

We evolve the full Einstein field equations using the Baumgarte-Shibata-Shapiro-Nakamura-Oohara-Kojima (BSSNOK) formulation of numerical relativity [19–21]. This formulation permits use of an arbitrary gauge and stress-energy source, allowing us to investigate the accuracy of linear theory in a cosmological setting for an arbitrary gauge, or slicing condition. We begin by writing two decompositions of the spacetime metric, the $3+1/\mathrm{ADM}$ form, and a linearized scalar-vector-tensor (SVT) decomposition,

$$\begin{aligned} g_{\mu\nu} &= \begin{pmatrix} -\alpha^2+\beta_l\beta^l & \beta_i \\ \beta_j & \gamma_{ij} \end{pmatrix} \quad (3+1) \\ &= \begin{pmatrix} -1 & \\ & a^2\delta_{ij} \end{pmatrix} + \begin{pmatrix} -E & a\partial_i F \\ a\partial_j F & a^2(A\delta_{ij}+\partial_i\partial_j B) \end{pmatrix} \\ &\quad + \text{vector} + \text{tensor}. \quad (\mathrm{SVT}) \end{aligned} \tag{1}$$

Here, γ_{ij} is the metric of a spatial hypersurface, and the parameters α and β^i are the lapse and shift, respectively. The lapse and shift are considered gauge variables, and may be freely chosen. The SVT scalars E, F, A, and B typically describe the dominant behavior of a spacetime, especially in a linearized gravity setting. Vector and tensor modes can formally contribute at linear order in a perturbative expansion, but respectively decay or remain small in commonly

used gauges unless sourced, and are therefore usually neglected in simulations of large-scale structures. We will not study these contributions here. The linearized Einstein equations are also found to provide independent equations for the scalar, vector and tensor modes.

Einstein's field equations can be written in terms of the metric, the extrinsic curvature K_{ij}, its trace K, and stress-energy source terms projected onto the spatial hypersurface as a system of first-order dynamical equations. Conformally related variants of these fields are evolved in the BSSNOK formulation. A conformal factor related to the determinant of the metric γ is also evolved, $\phi \equiv \ln(\gamma^{1/12})$, which we will refer to later. The metric fields and extrinsic curvature also satisfy the $3+1$ Hamiltonian and momentum constraint equations,

$$\begin{aligned} \mathcal{H} &= 0 = R + K^2 - K_{ij}K^{ij} - 16\pi\rho \\ \mathcal{M}^i &= 0 = D_j(K^{ij} - \gamma^{ij}K) - 8\pi S^i, \end{aligned} \tag{2}$$

where D_i and R are respectively the covariant derivative and Ricci scalar associated with the 3-metric γ_{ij}, and ρ and S^i are $3+1$ source terms, which are given by projections of the stress-energy tensor $T^{\mu\nu}$ onto spatial hypersurfaces,

$$\rho = n_\mu n_\nu T^{\mu\nu}, \qquad S_i = -\gamma_{ik} n_\mu = T^{k\nu}, \qquad S_{ij} = \gamma_{ik}\gamma_{jl}T^{kl} \tag{3}$$

with $n_\mu = (-\alpha, \vec{0})$.

For details on the code we use, see [22,23], or see [24,25] for a pedagogical introduction to numerical relativity, including further details on the formulation we use. Importantly, in the BSSNOK formulation as with numerical relativity formulations in general, some gauges will be more numerically stable than others. Slicing conditions commonly found in cosmology tend to be ill adapted for numerical evolution, including comoving-synchronous gauge, and relativistic generalizations of Newtonian gauge (see Appendix B).

To alleviate these problems, we sometimes use Z4c constraint damping while working in these gauges [26,27]. The Z4c formulation provides a prescription for modifying the BSSNOK formulation in order to tend the dynamical evolution of the metric towards obeying the nondynamical $3+1$ constraint equations. This does not guarantee better numerical convergence than the standard BSSNOK formulation, however, in some gauges it is able to suppress the growth of numerical error that would otherwise prohibit simulations from evolving stably at all. This formulation also provides an alternative to the constrained evolution scheme considered in [28], in which the conformal metric factor was solved (see also, e.g., [29]).

B. Matter evolution

In order to model dark matter, we primarily integrate the Einstein-Vlasov equations, modeled using an N-body system in harmonic and Newtonian gauges, and a perfect fluid in comoving-synchronous gauge. The Einstein-Vlasov equations describe a covariantly conserved phase-space density f along a trajectory described by an affine parameter λ,

$$\frac{Df}{d\lambda} = 0. \tag{4}$$

Simulations developed to solve this equation using N-body techniques within a general relativistic framework date back to seminal work in 1985 by Shapiro and Teukolsky [30], who examined the collapse of structures in a dimensionally reduced setting. Fully 3+1 N-body simulations appeared as early as 1999 [31,32], and have recently been employed in, e.g., studies of collapse [28,33]. For our N-body simulations, we employ a method similar to [28], making use of additional techniques in order to accelerate the numerical convergence of simulations. Additional schemes for modeling collisionless matter both approximately and using a fully relativistic treatment have been considered [8,24,34–38]; however a full review of these methods is beyond the scope of our work.

In comoving-synchronous gauge, we find poor convergence of simulations when using an N-body system. In this gauge, the particles do not move, so small errors sourced when we compute the density field from these particles can accumulate over time in a secular manner. This results in an unacceptably large amount of numerical error, preventing us from obtaining reliable results. We therefore use a perfect, pressureless fluid in synchronous gauge, which provides solutions equivalent in the continuum limit to an N-body simulation when no stream crossings are present.

The only variable that needs to be evolved for a pressureless fluid in comoving-synchronous gauge is the density. In particular, we can write a conservation equation for a conformally related density field $\tilde{D}$,

$$\partial_t \tilde{D} = \partial_t(\gamma^{1/2}\rho_0) = 0, \tag{5}$$

provided a rest-density ρ_0 and metric determinant γ. We provide further details on evolving this system in [22], and focus on describing N-body integration in the remainder of this section.

Rather than providing a fundamental description of particulate dark matter, N-body methods can be thought of as a way of discretizing a phase-space distribution in a manner suitable for numerical integration. This discrete representation becomes a solution to the Einstein-Vlasov equations in the continuum limit, as the spatial resolution and number of particles tend towards infinity, and particle deposition radius tends towards zero. We assume that the Einstein-Vlasov system provides a valid description of cold dark matter on a wide range of scales, down to scales of order interparticle spacing for particulate dark matter.

On smaller scales, or in scenarios where the density distribution is better described by pointlike matter sources, we may hope to gain fundamental insights into relativistic effects using, e.g., black hole lattice studies [36].

In a cosmological setting, it is common to start with a uniform density distribution in phase space that is "cold" (3-dimensional). We therefore begin by examining properties of a phase-space "sheet," a density distribution described by a 3-dimensional submanifold of 6-dimensional phase space. Locations on the sheet can be parametrized by coordinate labels, or a 3-vector $\vec{s}$. The coordinate location and velocity of each phase-space point in configuration space will be given by the functions $\vec{x}(\vec{s})$ and $\vec{u}(\vec{s})$, and the phase-space density $f(\vec{s}) = \text{const} \equiv \rho_s$ will be conserved for noninteracting, collisionless matter.

In order to determine how the fields $\vec{x}$ and $\vec{u}$ evolve at each point on the sheet, we can integrate the geodesic equations. In Newtonian gravity, these only require knowing the Newtonian potential, $\Phi_N(\vec{x})$, which in turn is determined by the metric-space density, $\rho(\vec{x})$, through Poisson's equation. In the relativistic case, the full metric is required, which is sourced by the $3+1$ stress-energy source terms. The problem is then to determine, given a phase-space distribution f, what the physical density is. The Newtonian density is given by the determinant of the Jacobian of the transformation between the two coordinate systems [39],

$$\rho(\vec{x}) = f(\vec{s}) / \det\left|\frac{\partial \vec{x}}{\partial \vec{s}}\right|. \tag{6}$$

Note that $\vec{x}(\vec{s})$ is not always invertible, or the Jacobian may be infinite at some points; the inverse function $\vec{s}(\vec{x})$ may also be multivalued, although $\vec{x}(\vec{s})$ should not be. For further discussion of this, we refer the reader to Appendix A and references therein.

Given this and a coordinate mapping $\vec{x}(\vec{s})$, we can determine $\rho(\vec{x})$. The standard Newtonian N-body prescription then discretizes the phase-space distribution at regular intervals of $\vec{s}$ into "particles" with a mass $m = \rho_s ds^3$, and considers the mass to be localized near a given metric-space coordinate $\vec{x}(\vec{s})$. The mass is assigned to a gridded metric-space density field using one of several mass deposition schemes. In standard N-body codes, perhaps the most common deposition scheme is the cloud-in-cell scheme, which assigns particle masses to a weighted average of nearby metric-space density grid cells, so that $\rho(\vec{x})$ is locally incremented by some amount m/dx^3 for each particle. We additionally implement a tricubic spline deposition scheme as described in [28]. Regardless of deposition scheme, in the limit of an infinite number of particles with infinitesimal mass, infinite resolution in metric space, and infinitesimal radius of deposition, Eq. (6) can be recovered.

General relativistic N-body systems extend this idea to a fully relativistic setting. For particles A with rest mass m_A, the source terms to the $3+1$ equations are given by [24]

$$\begin{aligned} \rho &= \sum_A m_A n_A W_A^2 \\ S_i &= \sum_A m_A n_A W_A u_i^A \\ S_{ij} &= \sum_A m_A n_A u_i^A u_j^A \\ S &= \gamma^{ij} S_{ij} = \rho - \sum_A m_A n_A \end{aligned} \tag{7}$$

where W is the relativistic Lorentz factor,

$$W_A = \alpha u^0 = \sqrt{1 + \gamma^{ij} u_i u_j}, \tag{8}$$

and n_A is the relativistic volume element,

$$n_A = \frac{1}{W_A \gamma(x_A)^{1/2} dx dy dz}. \tag{9}$$

Equation (6) also picks up a factor of $\sqrt{\gamma}/W$ on the left-hand side of the equation [e.g., Eq. (A2)]. The geodesic equations can be neatly written in terms of covariant spatial velocities and contravariant coordinates,

$$\begin{aligned} \frac{du_i}{dt} &= -\alpha u^0 \partial_i \alpha + u_j \partial_i \beta^j - u_j u_k \partial_i \gamma^{jk} \\ \frac{dx^i}{dt} &= \gamma^{ij} \frac{u_j}{u^0} - \beta^i, \end{aligned} \tag{10}$$

where u^0 is given in terms of u_i in the expression for W above. Using this prescription, we can evolve u_i and x^i at each point s^i according to the geodesic equations, and compute the density and other stress-energy source fields using Eq. (7). In the Newtonian limit where $u_i \ll 1$ and $\alpha = 1 + \Phi_N$ with $\Phi_N \ll 1$, the geodesic equations reduce to the Newtonian ones, with $\partial_t u_i = -\partial_i \Phi_N$ and $\partial_t x^i = u^i$.

One of the drawbacks of N-body methods is the presence of sampling noise in the stress-energy source fields, which in turn sources noise in the metric fields. To alleviate this, phase-space element techniques have recently been developed [39,40]. One explicit implementation of these methods is to interpolate additional particles in the phase-space distribution: the fields x^i and u_i are known on a grid described by coordinates s^i, and can there be interpolated to arbitrary s^i, providing a way to deposit additional particles for which the geodesic equations are not explicitly used to evolve. We take advantage of this, using tricubic interpolation, depositing additional appropriately weighted masses in order to increase the smoothness of the density field, and depositing all particles according to Eq. (7).

C. Initial conditions

Synchronous gauge is the only gauge we use that requires a fixed choice of lapse and shift on the initial surface. The other gauges we utilize are driver gauges, which impose conditions only on the time evolution of the lapse, and can thus be initialized with the same lapse and shift as synchronous gauge; their subsequent evolution will be "driven" towards a particular slicing condition irrespective of the initial hypersurface chosen. We therefore choose conditions with an initial lapse and shift given by the synchronous gauge ones,

$$\alpha = 1, \qquad \beta^i = 0. \tag{11}$$

We then need to solve the Hamiltonian and momentum constraint equations (2). A choice for the metric itself can be made using the Zel'dovich approximation [41]. In Newtonian gauge, where $\Phi_N \equiv E/2$ and $\Psi_N \equiv -A/2$, the Zel'dovich approximation sets the time derivative of the Newtonian potential to zero, $\dot{\Phi}_N = 0$. Synchronous gauge potentials that coincide with this choice in linear theory can be chosen,

$$A = \Phi_N, \qquad \dot{A} = B = \dot{B} = 0, \tag{12}$$

and from the linearized Einstein's equations in absence of anisotropic stress we also find

$$\ddot{B} = A, \tag{13}$$

from which we can also derive the relation $\Phi_N = \Psi_N$. A choice of constant trace of the extrinsic curvature, $K = \text{const}$, can then be made to produce a desired background evolution. Once given this choice of metric, the density ρ and momentum S^i can be solved for using the constraint equations, and this solution will coincide with the Zel'dovich approximation in comoving-synchronous gauge at linear order, but will now satisfy the full, nonlinear constraint equations.

We additionally need to determine the primitive stress-energy source variables, not just the $3+1$ sources. Given an arbitrary metric, this can be accomplished algebraically prior to stream crossing when the stress-energy tensor of various components of the Universe, including collisionless matter and a cosmological constant, coincide with that of a perfect fluid,

$$T^{\mu\nu} = (\rho_0 + P)u^\mu u^\nu + P g^{\mu\nu}, \tag{14}$$

with equation of state $P = w\rho_0$. The $3+1$ source terms for this stress-energy tensor are given by

$$\rho = (\rho_0 + P)W^2 - P, \tag{15}$$

$$S_i = \gamma_{ij} S^j = (\rho_0 + P) W u_i. \tag{16}$$

For multiple species, the stress-energy tensor will be given by the sum of individual contributions from all species $\mathcal{S}$,

$$T^{\mu\nu} = \sum_{\mathcal{S}} T^{\mu\nu}_{\mathcal{S}}, \tag{17}$$

and the contribution from each species to the $3+1$ sources will be given by $\rho = \sum_{\mathcal{S}} \rho_{\mathcal{S}}$ and $S^i = \sum_{\mathcal{S}} S^i_{\mathcal{S}}$. Once given a metric, the constraint equations provide a prescription for ρ, however additional information is required in order to specify the contributions of each species. In the case of a cosmological constant and collisionless matter, $\mathcal{S} \in \{m, \Lambda\}$, we can divide ρ into two pieces, respectively a constant ρ_Λ, and the remainder $\rho_m = \rho - \rho_\Lambda$.

Once $\rho_{\mathcal{S}}$ and $S^i_{\mathcal{S}}$ are determined for each species, the matter sources can be solved algebraically for the primitive fluid density and velocity fields, $u^i_{\mathcal{S}}$ and $\rho_{0,\mathcal{S}}$. For a cosmological constant Λ, the equation of state parameter will be $w = -1$, and the solution is necessarily $\rho_{0,\Lambda} = -P_\Lambda = \rho_\Lambda = \text{const}$. For a more general fluid with $w \neq -1$, a solution for $W^2_{\mathcal{S}}$ is given by

$$W^2_{\mathcal{S}} = \frac{1 - 2C_{\mathcal{S}}R_{\mathcal{S}} + \sqrt{1 + 4R_{\mathcal{S}}C_{\mathcal{S}}(R_{\mathcal{S}} - 1)}}{2(1 - C_{\mathcal{S}})}, \tag{18}$$

with

$$R_{\mathcal{S}} = \frac{w}{1+w}$$
$$C_{\mathcal{S}} = \gamma_{ij} S^i_{\mathcal{S}} S^j_{\mathcal{S}} / \rho^2_{\mathcal{S}}. \tag{19}$$

Equation (15) can be subsequently solved for $\rho_{0,\mathcal{S}}$ and Eq. (16) solved for $u_{i,\mathcal{S}}$. This approach to setting initial conditions remains valid for an arbitrary equation of state parameter w, including the case of an N-body system in absence of stream crossings. For such collisionless matter or a $w = 0$ fluid, the solution reduces to $C_m = 0$, $W^2_m = 1$, and $\rho_m = \rho_{0,m}$, again consistent with linear theory.

The final solution we obtain for collisionless matter and a cosmological constant is then determined. Given an initial Φ_N and constants K and $\rho_\Lambda/\rho = \Omega_\Lambda$, we have

$$\gamma_{ij} = (1 - 2\Phi_N)\delta_{ij} \qquad \rho_{0,\Lambda} = \Omega_\Lambda \rho$$
$$K^{\mathrm{TF}}_{ij} = u_{i,m} = 0 \qquad \rho_{0,m} = (1 - \Omega_\Lambda)\rho, \tag{20}$$

where $16\pi\rho = R + 2K^2/3$. In order to determine ρ in practice, we specify the BSSNOK conformal variable ϕ as the solution to $e^{4\phi} \equiv \gamma^{1/3} = 1 + A = 1\text{–}2\Phi_N$. Once we have the metric and density field $\rho_{0,m}$, we can find a Jacobian transformation that satisfies Eq. (6) in order to set initial particle positions.

Often in numerical literature, additional physical perturbations are introduced on small scales as numerical resolution is increased. This procedure can result in

confusion between numerical effects and new physics, leading to difficulty verifying the numerical accuracy of results, especially when we are interested in resolving corrections that can have quite small amplitudes. We therefore opt to study solutions initially described by a single mode in one dimension, and three modes in three dimensions, and to verify formal numerical convergence of our solutions with a fixed physical construction.

Some progress can be made analytically determining particle displacements for a given density field, allowing us to obtain initial conditions efficiently, as well as to benchmark the accuracy of a more general solver. Determining a displacement field is difficult in general, as it requires the density field be both analytically integrable and invertible. We can nevertheless write down an analytically integrable density field that is a solution to the constraint equations, in which case determining particle displacements is reduced to a root-finding problem. We choose the conformal factor ϕ to be

$$\phi = \log[1 + A\sin(2\pi x/L)] \tag{21}$$

and the extrinsic curvature (expansion rate) $K = K_{\mathrm{FLRW}}$ to determine the density field using Eq. (20). The integral of the density field can then be written,

$$\begin{aligned}\int dx\sqrt{\gamma}\rho_{0,m}(x) = \frac{1}{1920\pi L^2}\Bigg[&120\pi x(16\pi A^2 + (5(A^4 + 18A^2 + 24)A^2 + 16)L^2\bar{\rho}_m) \\ &+ AL\Bigg(A\Bigg(L^2\bar{\rho}_m\Bigg(-5A^4\sin\left(\frac{12\pi x}{L}\right) - 72A^3\cos\left(\frac{10\pi x}{L}\right) + 45(A^2+10)A^2\sin\left(\frac{8\pi x}{L}\right) \\ &+ 200(3A^2+8)A\cos\left(\frac{6\pi x}{L}\right) - 225(A^4 + 16A^2 + 16)\sin\left(\frac{4\pi x}{L}\right)\Bigg) - 480\pi\sin\left(\frac{4\pi x}{L}\right)\Bigg) \\ &- 240(3(5(A^2+4)A^2+8)L^2\bar{\rho}_m + 8\pi)\cos\left(\frac{2\pi x}{L}\right)\Bigg)\Bigg] \\ \simeq \bar{\rho}_m x - \frac{A(3L^2\bar{\rho}_m + \pi)}{\pi L}&\cos\left(\frac{2\pi x}{L}\right) + \mathcal{O}(A^2),\end{aligned} \tag{22}$$

where $\bar{\rho}_m = (1.0 - \Omega_\Lambda)K^2/24\pi$, and from which the displacement field, $x(s)$, is determined.

For more generic initial conditions, especially in three spatial dimensions, we require a method to displace particles to reproduce an arbitrary density field. In standard N-body simulations, displacements are commonly computed within perturbation theory. However, such a solution will not obey the constraint equations exactly, resulting in a small but measurable amount of violation of the full GR constraint equations.

A more general way of ensuring the constraint equations are fully satisfied is a diffusion method, in which particles are drifted until a desired density field is produced. The idea behind this method has been used in the past in various settings, for example equalization of cartographic data according to properties such as population density [42]. We begin with an approximate guess of particle positions $x^i_g(s^i)$ which generate a density field ρ_g, and adjust particle positions in order to send $\rho_g \to \rho_{0,m}$. Phrased in terms of the difference of these, we wish to equalize $\Delta\rho \equiv \rho_{0,m} - \rho_g$, so that $\Delta\rho \to 0$. We can drift particle positions along gradients in the field $\Delta\rho$ according to

$$\dot{x}^i_g = \eta_D \partial_i(\Delta\rho), \tag{23}$$

for a given diffusion strength η_D. The coefficient η_D needs only be chosen so that the solution converges; larger values of η_D may result in faster convergence, but can also result in instabilities if particles "overshoot" final positions along their trajectories.

D. Gauge choices

In this section we review some common gauge choices, drawing parallels between gauge choices in approximate treatments and fully relativistic counterparts in a $3+1$ language. We therefore examine two common gauge choices, comoving-synchronous gauge and a quasi-Newtonian gauge, in addition to the harmonic slicing condition commonly used in numerical relativity.

We begin by noting that the results we obtain are not observables in the sense that our results may vary between these gauges. How accurately we can compute what a particular class of observers would see, such as observers chosen to be normal to given spatial hypersurfaces defined by a particular time slicing or gauge, will depend on the accuracy with which quantities can be computed that gauge. However, the set of observers chosen to measure observables in a cosmological setting are often chosen to coincide with a background, reference FLRW metric, and so observables will generally be gauge independent.

They will still depend on how this background is chosen, which is ambiguous beyond linear order.

Comoving synchronous gauge (also referred to as geodesic slicing, and which is referred to more concisely as "synchronous gauge" throughout this work) is well defined in both a fully relativistic setting and in linear theory, i.e., can be defined without requiring approximations. This choice corresponds to

$$\alpha = 1, \qquad \beta^i = 0 \tag{24}$$

in a $3+1$ language, or choosing $E = 0$ and $F = 0$ in the SVT language. Some remaining ambiguity exists in how the potentials A and B are chosen, although this is irrelevant as long as observables are computed in the end. While we do not compute observables in this work, this ambiguity remains irrelevant insofar as we are interested in studying the accuracy of linear theory in describing relativistic properties of the spacetime in specific gauges, rather than drawing conclusions about physical quantities or observables.

Harmonic slicing can be viewed as a foliation that tends to evolve towards maximal slicing, or a driver condition for maximal slicing, where maximal slicing is defined by choosing a lapse such that $K = 0$ [43]. This gauge choice coincides with the time slicing used in the harmonic formulation of Einstein's equations, where coordinates themselves satisfy $\Box x^\mu = 0$. However, we maintain zero shift, so the condition is not entirely equivalent. In a FLRW setting, this condition is also modified so that rather than being driven to zero, the value of K will be driven to that of a reference FLRW value [44]. A constant-K condition is sometimes referred to as a uniform expansion gauge; here we are considering a driver version which can approximate this condition. The resulting expression is

$$\partial_t \alpha = -\eta_H \alpha^2 (K - K_{\mathrm{FLRW}}), \tag{25}$$

where K_{FLRW} is the trace of the extrinsic curvature we wish to drive towards, and can be freely chosen. We use a coefficient $\eta_H = 1$ as is common, but also note that as $\eta_H \to \infty$, uniform expansion should be recovered, reducing to the maximal slicing condition when $K_{\mathrm{FLRW}} = 0$ [24]. The constant-K limit has also been studied in detail in a linearized cosmological setting in [16].

Lastly, we wish to consider a gauge analogous to Newtonian gauge, commonly found in a linearized, scalar-only context [45]. This condition can be imposed on the scalar part of the metric by setting the scalar potential $B = 0$, or choosing the scalar part of K_{ij} to be purely traceful. Unfortunately, although we refer to this gauge as "Newtonian" in order to make the analogy explicit, there is no exact generalization of Newtonian gauge in a fully relativistic setting. A more general choice is to impose a zero-shear (or "isotropic expansion") condition on the spatial metric [46]; however, this condition relies upon both a choice of background and an assumption of linearity. A relativistic generalization of this condition would involve imposing this condition on the anisotropic contributions to the extrinsic curvature, requiring

$$K^{ij}_{\mathrm{TF}} = 0, \tag{26}$$

however not enough gauge freedom exists to fully enforce this condition. Instead, we consider a minimal-shear driver condition in order to reproduce the zero-shear condition to some approximation. Our choice of this minimal-shear condition is given by

$$\partial_t \alpha = \eta_G \left(\frac{2}{3} \nabla^2 \alpha - \frac{1}{\nabla^2} \sum_{i,j} \partial_i \partial_j R^{\mathrm{TF}}_{ij} \right), \tag{27}$$

which we derive and explore additional properties of in Appendix B, and for which we will extrapolate to the $\eta_G \to \infty$ limit. Although we refer to this as Newtonian gauge, a more appropriate name is perhaps a "minimal-shear driver gauge."

III. RESULTS

We now proceed to examine the accuracy of linear theory in several ways. We do so by numerically obtaining full, general relativistic solutions, and examining to what degree the linearized Einstein field equations are satisfied. In particular, we check the linearized, trace-free spatial part of Einstein's equations,

$$G^{\mathrm{TF}}_{ij} - 8\pi T^{\mathrm{TF}}_{ij}. \tag{28}$$

For a universe containing only collisionless matter and dark energy, the scalar contributions to this equation give rise to the expression [15]

$$\begin{aligned}(\partial_i \partial_j)^{\mathrm{TF}} \mathcal{V} &\equiv (\partial_i \partial_j)^{\mathrm{TF}} (E + A - a^2 \ddot{B} - 3a\dot{a}\dot{B} + 2a\dot{F} + 4\dot{a}F) \\ &\simeq 0.\end{aligned} \tag{29}$$

Involving no matter terms at linear order for cold dark matter and a cosmological constant, this constraint can be viewed as purely gravitational, expected to remain valid even in the presence of large density contrasts so long as the metric potentials themselves are small. Neglected stress-energy contributions to $\mathcal{V}$ come from anisotropic stress, and are of order $\mathcal{O}(v^2/\partial^2)$. In comoving-synchronous gauge where $E = F = 0$, this expression places a constraint on the potentials A and B, while in a Newtonian setting where $B = F = 0$, this enforces $E = A$, or $\Phi_N = \Psi_N$, a condition explicitly enforced in much of cosmological literature. Violation of this constraint is referred to as gravitational slip, and has been characterized using perturbative and weak-field approaches [47,48]. Slip is also looked for as a

signature of modified gravity models [49]. However, given an exact solution to Einstein's equations, the linear constraint equations will not be perfectly satisfied; it is therefore important to check how well this expression holds lest an observed violation be mistaken as a sign of failure of general relativity.

We directly report the violation $\mathcal{V}$ relative to the root sum of the squares of the terms comprising it, which we denote $[\mathcal{V}]$. This is opposed to its Hessian as found in Eq. (29), which is not often directly utilized; this ratio also disguises the precise amplitude of $\mathcal{V}$, so we note that we find general consistency with it being of order h. There is freedom to choose the zero mode of B up to an arbitrary time-dependent function; we choose this to be zero. This quantity will still depend on the FLRW background chosen, so we note that we use averaged quantities to construct a and its time derivatives, in order to decouple the sensitivity of this expression to the question of how closely averaged quantities follow a FLRW model.

We can nevertheless explore this last point, sometimes referred to as the fitting problem or "backreaction," by checking to see how well FLRW model parameters agree with spatially averaged quantities. We explore this question by looking at the average expansion rate on spatial slices and comparing to the expected FLRW value,

$$\mathcal{K} \equiv 1 + 3\frac{H_{\mathrm{FLRW}}}{\langle K\rangle} \simeq 0, \tag{30}$$

where the average is volume weighted,

$$\langle K\rangle = \frac{\int d^3x\sqrt{\gamma}K}{\int d^3x\sqrt{\gamma}}. \tag{31}$$

This quantity will of course depend on the chosen slicing condition—here, we are interested in the degree to which $\langle K\rangle \simeq -3H_{\mathrm{FLRW}}$ in gauges commonly used for interpreting cosmological dynamics. Although we do not directly compute observables in this work, should an observable coincide with the choice of gauge (e.g., the proper time observable [50] coincides with the proper time slicing condition of synchronous gauge), the results we present can contain implications for observable quantities.

We also compare results to the metric perturbation amplitude h by computing

$$h \equiv \frac{1}{3}(\mathrm{perm}|\bar{\gamma}_{ij}| - 1), \tag{32}$$

with $|\bar{\gamma}_{ij}| = |\gamma_{ij}|/\gamma^{1/3}$, which is the absolute value of the conformally related BSSNOK metric, and perm, the permanent matrix operator, which we use to reduce the expression to an overall measure of magnitude.

Literature largely anticipates that cosmological systems are well described by linear theory on scales larger than $\mathcal{O}(10)$ Mpc, albeit with appreciable mode coupling on scales up to $\mathcal{O}(100)$ Mpc due to nonlinearities, and excepting extreme large-scale structures which we will examine later. In Newtonian gauge, nonlinearities are attributed solely to dynamics of the matter sector rather than the gravitational sector, so δ_ρ can be large while h remains small. As our interest is in the gravitational sector, we have chosen to measure the accuracy of standard linear calculations using Eq. (29), which is expected to hold even in the presence of large, $\mathcal{O}(1)$ density perturbations in Newtonian gauge. In synchronous gauge, the amplitude of metric perturbations is not suppressed relative to the density contrast, and we do not expect suppression of metric perturbations relative to density perturbations on these scales, so considerable violation may appear.

We will consider scales on which we can obtain a satisfactory answer in all the gauges we consider. In particular, we examine modes of wavelength $L \gtrsim 35$ Mpc. On the other hand, the largest observable scales are of order the current Hubble scale, $H_0^{-1} \sim 4.4$ Gpc, so we will also consider modes up to this scale. We run a suite of planar-symmetric ("mode in a box") simulations across this range of scales. We then extend our results to full, asymmetric 3D simulations with two goals: first, we examine the applicability of the planar-symmetric results to a more general context by comparing the amplitudes $\mathcal{V}$ and $\mathcal{K}$ between a three-dimensional and planar-symmetric setting, and second, we consider modes with larger-than-typical amplitudes in the full 3D case, motivated by observations of extremely large structures.

A. Benchmarks in a planar-symmetric setting

The planar-symmetric simulations we run begin at a redshift $z \simeq 50$, when the energy density of the Universe is dominated by cold dark matter in the concordance cosmology. We run all simulations with initial conditions as described in Sec. II C, using identical initial conditions in all gauges. We determine the initial amplitude of density perturbations using CAMB to compute the synchronous gauge density power spectrum $P_{\delta\delta}(k)$ [51], from which we compute rms density perturbation amplitudes smoothed on a length scale L,

$$\frac{\sigma^2_{\rho,L}}{\bar{\rho}^2} = \frac{1}{2\pi^2}\int k^2 e^{-(kL)^2} P_{\delta\delta}(k)dk. \tag{33}$$

We use CAMB settings including the halofit nonlinear matter power spectrum, $H_0 = 67.5$, $\Omega_b h^2 = 0.022$, $\Omega_c h^2 = 0.122$, $n_s = 0.965$, and otherwise default settings to compute $\sigma_{\rho,L}$, and choose mode amplitudes so the RMS density perturbations agree with this value.

The planar-symmetric runs have a metric grid resolution of $N_x = 64$, 96, 128 with $N_y = N_z = 1$, and number of particles $N_p = N_x^2/8$. We generally find 2nd-order

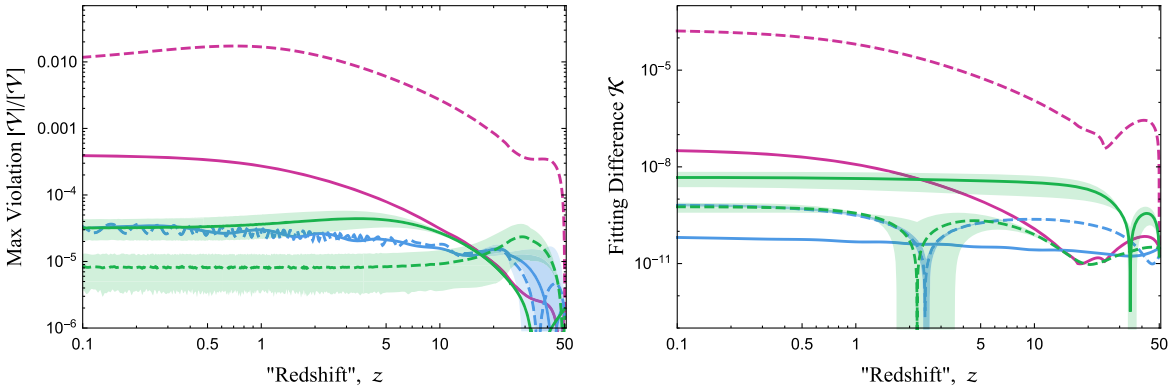

FIG. 1. Accuracy of approximations for two "modes" with concordance cosmology amplitudes in different gauges. The left plot shows the evolution of the maximum violation of the linearized Einstein equations, Eq. (29), and the right the evolution of the fitting difference, Eq. (30). Synchronous gauge results are shown in pink, harmonic in blue, and Newtonian in green. Solid lines indicate results for a ∼1 Gpc mode wavelength, and dashed for a ∼100 Mpc mode. Confidence intervals are indicated for all results using shaded bands, and are not visible when sufficiently small. The Newtonian curves have been extrapolated to the $\eta_G \to \infty$ limit as described in Appendix B.

convergence in the case that error due to particle deposition dominates, and 4th-order convergence for large physical box sizes in which case time stepping error dominates. Finite differencing is 8th order, and is not found to be the dominant source of error for particle runs, but can be for the fluid simulations in synchronous gauge. Our final results are Richardson extrapolated using all pairs of resolutions, and numerical confidence intervals inferred from the remaining disagreement between extrapolated values. We provide further discussion and details of numerical convergence in Appendix C.

We first examine the degree of violation of the linearized Einstein equations as described by $\mathcal{V}/[\mathcal{V}]$ in Eq. (29). We show the maximum absolute value of the violation in different gauges in Figs. 1 and 2. The results we find are consistent with the expectation that $\mathcal{V} \sim \mathcal{O}(h^2)$ and $[\mathcal{V}] \sim \mathcal{O}(h)$, so that $\mathcal{V}/[\mathcal{V}] \sim \mathcal{O}(h)$. Importantly, the degree of violation is found to be scale dependent and gauge dependent, and in fact the violation can be quite large in synchronous gauge where h is of order δ_ρ, implying the metric given by linearized calculations in synchronous gauge will not be accurate when sufficiently small ("nonlinear") scales are considered.

We examine both the time dependence of modes and the scale dependence of solutions at the end of the runs. The time dependence is expressed in terms of the FLRW redshift function of the BSSN conformal factor as

$$z = \exp\left[2\langle\phi_{\text{final}}\rangle - 2\langle\phi\rangle\right] - 1. \tag{34}$$

Several features can be seen in both the time-dependence and scale-dependence plots. We interpret these as transients due to physics in the gauge, initial conditions which are not purely growing mode solutions, or, especially at early

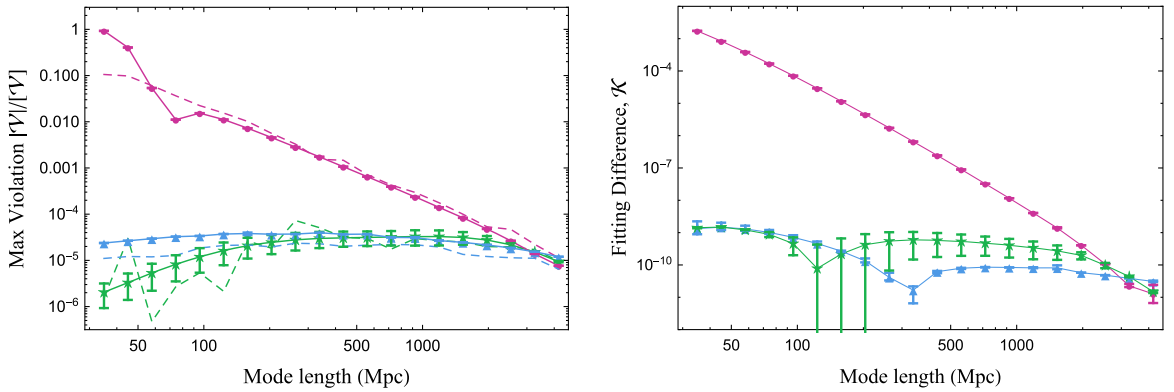

FIG. 2. The accuracy of approximations is shown in various gauges as a function of mode wavelength, for concordance cosmology mode amplitudes. Synchronous gauge results are shown in pink circles, harmonic in blue triangles, and Newtonian (see Appendix B) in green stars. Results include numerical confidence intervals and are connected by a solid line, while dashed lines indicate the amplitude h [Eq. (32)]. The left plot shows the difference between a background FLRW Hubble parameter and averaged expansion rate, and the right plot shows the violation of the linearized Einstein equations.

times, the system transitioning from the synchronous gauge solution to the preferred slicing in the driver gauges. Despite the specific dynamics giving rise to these features, we expect that the order of magnitude of these results is fairly insensitive to the precise initial conditions used.

Turning to examine the overall trends, we indeed find appreciable linearized constraint violation in synchronous gauge on scales when nonlinear dynamics begins to become important, or when $\sigma_\rho/\bar{\rho}$ is no longer small. We generally find harmonic slicing results to be consistent with small second-order corrections: violation amplitudes remain below 10^{-4} at all times, in line with expectations from field values h. The inexact nature of Newtonian gauge provides us with a more complicated story, which we provide detail on in Appendix B, however agreement is still found in this case. As a final note, there is some expectation that a minimal-shear gauge will behave poorly on large scales, leading to divergent mode amplitudes. While we have considered these scales, we have circumvented this difficulty by initializing our simulations in synchronous gauge, which are then driven towards other slicings, and may not have sufficient time to appear. In contrast to the minimal-shear condition, synchronous gauge is well behaved on large scales, so there is no such subtlety setting initial conditions. The $\eta_G \to \infty$ extrapolation also results in appreciable error in our Newtonian-gauge results, while other numerical errors are considerably smaller, as seen in other gauges.

We also examine the same data, but check how the degree to which averaged quantities agree with FLRW quantities. We find results generally consistent with those seen in the time evolution: the behavior of the Synchronous gauge metric is not well described by a background FLRW behavior, while the harmonic and Newtonian-gauge metrics are. We may particularly expect that the fitting difference in harmonic slicing to be small, due to the gauge condition explicitly driving the solution towards that of a FLRW spacetime. The Newtonian and synchronous gauge results are also qualitatively consistent with prior literature looking at backreaction using a partially nonlinear treatment [18], although we do not resolve scales as small as that work due to the breakdown of synchronous gauge in a fully relativistic setting, and also expect a fully relativistic calculation to be necessary in such a nonperturbative setting.

The fitting difference in synchronous and harmonic slicings has also been examined using fully relativistic simulations [10,14,18]. In these studies, backreaction in the sense of violation of the FLRW acceleration equation was been found to be small, while properties of hypersurfaces such as the average volume or average expansion rate could show larger deviations from the average, especially in synchronous gauge.

Because the way we measure the fitting difference is gauge dependent, the results we present here, and indeed results found in any gauge, are only meaningful to either the extent that these quantities describe observables, or that these quantities are used as an intermediary step to computing observables. To that end, it is interesting to consider that synchronous gauge coincides with a proper time slicing, making it possible, at least in principle, to pick out spatial hypersurfaces in this gauge. Newtonian and harmonic slicing conditions, on the other hand, do not so neatly determine an observable; no (fully nonlinear) observable properties of a spacetime coincide with the foliations. Rather, observables are usually constructed from contributions to the metric and matter fields whose physical interpretations are gauge dependent.

As a final point, we note that backreaction has also been looked at in harmonic slicing in the context of black hole lattice simulations. While the expansion properties of these systems has been found to reproduce FLRW behavior to some approximation [52–54], it has also been shown that the averaged optical properties of these spacetimes do not always coincide with expectations from a FLRW model, even in a homogeneous limit [55]. A necessary next step will therefore be examining optical properties of inhomogeneous spacetimes in a fully relativistic context, especially in the limit that inhomogeneities are introduced and localized on increasingly small scales.

B. Benchmarks in a general 3D setting

As an exploration of over/underdensities with scales similar to the largest observed structures in our Universe, as well as checking that the results we find in the planar-symmetric runs are indicative of the order of magnitude of corrections in a less symmetric setting, we additionally run fully 3-dimensional simulations in harmonic and synchronous gauges. When including perturbations in additional dimensions we have some expectation that the violation amplitude can increase: collapse can now occur in these additional directions, allowing field profiles to further deviate from their original modelike profiles than in the 1-dimensional case.

We initialize these simulations at redshift $z = 5$ as a superposition of modes. We follow the prescription described in Eq. (20), but now using the diffusion method to determine initial particle displacements. The BSSNOK conformal factor is chosen to be

$$\phi = \sum_i A \sin(2\pi x^i/L), \tag{35}$$

where the sum over i is a sum in each direction.

In order to choose relevant and interesting length and overdensity scales, we consider the case of particularly large voids and overdensities. For typical overdensity amplitudes on a wide range of scales, there is the expectation that nonlinear corrections are small in appropriately chosen gauges and a perturbative approach is therefore well justified [56], something we have explicitly confirmed above. However, uncommon structures with large density

contrasts have been observed on large scales in our Universe, for example [57–59], along with even larger but more controversial structures. The density contrast in these regions can reach tens of percents or more on length scales of up to a few hundred Mpc. We first use a simulation with parameters comparable to the void described in [59]. The diameter of this supervoid is of order 400 Mpc, and density contrast optimistically of order $\delta_\rho \sim -0.2$. We therefore simulate a box with $L \sim 400$ Mpc and $\sigma_\rho/\bar{\rho} \sim 0.2$ at the end of the simulation. We also run a $L \sim 100$ Mpc simulation with $\sigma_\rho/\bar{\rho} \sim 1$, comparable to parameters of the Sloan Great Wall described in [58], which has an effective radius of order 50 Mpc and reported mass excess δ_M larger than unity.

We naively expect the metric perturbation amplitude for these runs to be of order $\Phi_N \sim 4\pi G L^2 \rho \sim 10^{-3}$. We do not run full, 3D simulations in Newtonian gauge due to the poor numerical properties of the gauge, but anticipate given our earlier results and additional 1D tests that fractional corrections to the Newtonian potential are comparable to harmonic gauge. On the other hand, we expect the synchronous gauge potentials to be closer to $\sigma_\rho/\bar{\rho}$.

We run the fully 3-dimensional simulations for the above choices of L and σ_ρ, along with planar-symmetric simulations using the same physical parameters in order to compare results. The synchronous gauge runs utilize a number of grid points $N^3 = 24^3, 32^3, 40^3$ for all 3-dimensional runs, and $N = 64$, 96, 128 for all planar-symmetric runs. In harmonic gauge for the 3-dimensional, $L = 100$ Mpc runs, we use $N^3 = 16^3, 20^3, 24^3$ metric grid points with $N_p = (4N)^3$ particles, and $N^3 = 24^3, 28^3, 32^3$ with $N_p = (N^2/4 - 2N)^3$ particles for the $L = 400$ Mpc runs. For the planar-symmetric comparisons, we use $N = 24$, 28, 32 with $N_p = N^2/2 - 8N$, although we also run with higher resolutions as described in Sec. III A in order to examine accuracy and for the Newtonian-gauge comparison. We encounter some difficulty extrapolating Newtonian results to the $\eta_G \to \infty$ limit for the fitting difference as zero-crossing locations are sensitive to the driver coefficient, resulting in a large uncertainty in the

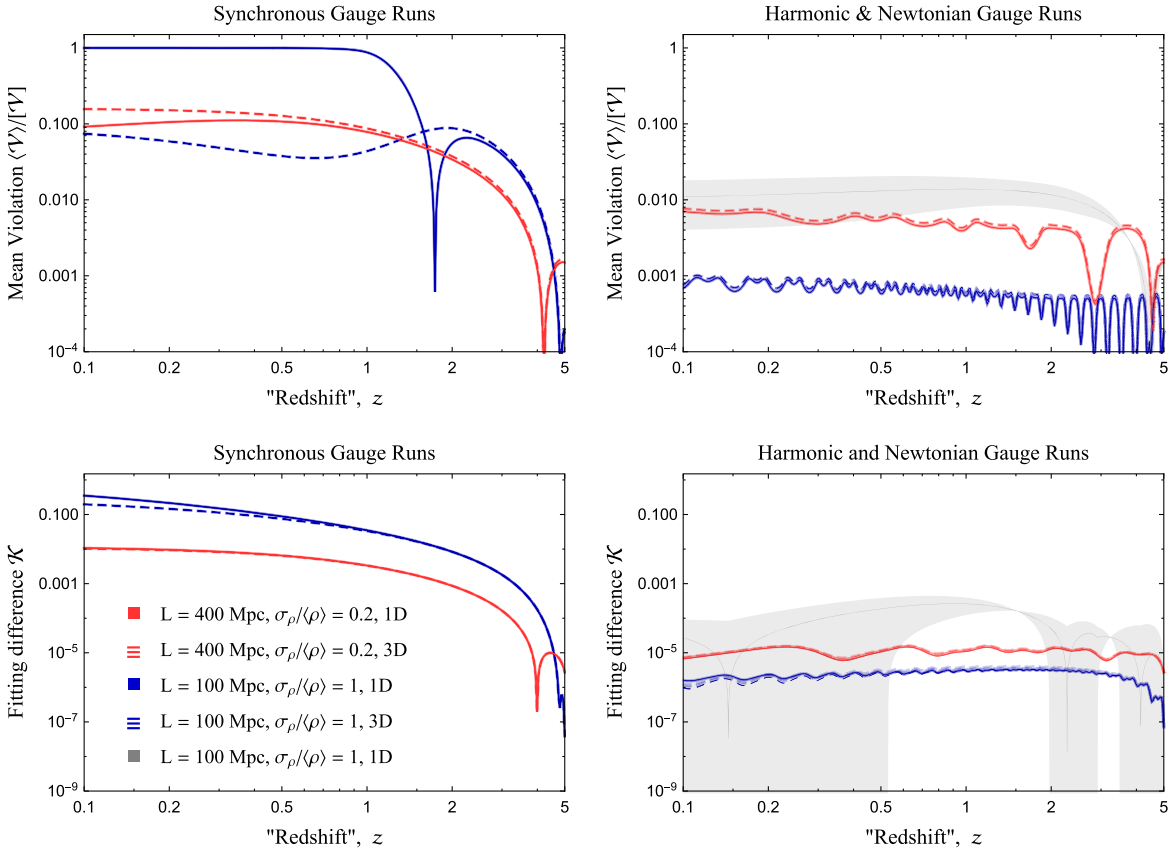

FIG. 3. We show the mean violation $\langle \mathcal{V} \rangle / [\mathcal{V}]$ and fitting difference $\mathcal{K}$, for planar-symmetric ("1D," solid) and asymmetric ("3D," dashed) runs, in synchronous and harmonic gauges as indicated by plot titles, for the large void (red) and overdensity (dark blue), as a function of FLRW redshift. For comparison, the light gray line and band are results and uncertainty from a planar-symmetric simulation using void parameters in Newtonian gauge. Values from individual runs at different resolutions are indicated by thick, light bands, and Richardson extrapolated values by thin, darker lines. Near-perfect agreement is found in harmonic and synchronous gauges, so individual runs and extrapolated values are nearly indistinguishable.

precise behavior of $\mathcal{K}$. We provide further details on the convergence of these runs in Appendix C, and show results from these runs in Fig. 3.

For these runs, we find corrections to linear theory can surpass the expected 10^{-3} level in harmonic and Newtonian gauge and reach the percent level. This is still within a perturbative regime, but suggests nonlinear gravitational effects are unexpectedly beginning to become important for these extreme structures, regardless of gauge. These nonlinear effects may be important to properly model in order to draw accurate inferences for cosmology and for astrophysics of these extreme structures. In synchronous gauge, the corrections become tens of percent up to order unity, indicating the failure of a perturbative approach to be able to describe the synchronous gauge metric. We also find that the violation amplitudes in the 3-dimensional cases are comparable to the planar-symmetric runs, and thus we expect the planar-symmetric results provide a good indication of the level of linearized constraint violation.

IV. CONCLUSIONS AND DISCUSSION

We have examined the magnitude of violations in a standard cosmological setting using fully relativistic simulations, and found support for the idea that relativistic corrections scale as $\mathcal{O}(h^2)$ on large scales. The magnitude of h itself will be gauge dependent, will not always be small depending on the gauge in question, and can be appreciable in any gauge for sufficiently extreme structures. For codes that work in synchronous gauge in a linearized context, such as CAMB or CLASS when run in synchronous gauge, it is therefore inaccurate to directly infer properties of metric and matter fields in synchronous gauge. However, because the results of these calculations can be considered as identical to calculations in a well-behaved gauge under a change of variables, observables computed from these codes can still be recast as having been performed in a gauge where nonlinear gravitational effects are small.

It is still important to note that we have not directly computed any observable quantities, except according to particular classes of observers defined by specific time slicings. Rather, we have examined the accuracy of intermediate steps used in approximate calculations. The physical interpretation of the various fields involved will be gauge dependent in general: for example, peculiar velocities and matter power spectra will depend on the chosen slicing. The accuracy with which these effects can be interpreted is subject to gauge, and as a consequence so are the precise values of inferred cosmological parameters describing properties of these spacetimes. True observables can still be constructed by projecting these fields onto past null geodesics. Relativistic effects involved in this projection are not trivial to compute, although recent progress has been made both analytically and numerically [9,60]. We can expect that the accuracy of these projections in a perturbative context will also depend on gauge: light cones in comoving-synchronous gauge (Lagrangian frame) can contain quite large distortions, while these effects will be smaller but still important in, e.g., Newtonian gauge (Euclidean frame). Observables computed in linear theory are gauge invariant only at linear order, and even then linear gravitational effects are often neglected due to physical or practical considerations in particular gauges. As a consequence, these observables and corresponding average properties of the spacetime are perhaps best interpreted as having been computed under a change of variables in a gauge that maximally satisfies any approximations made, for example N-body gauge in the case of Newtonian N-body simulations [61].

We are also mindful of the assumptions we have made in this work. It will be important to work towards relaxing the coarse-graining operation implicitly performed when utilizing a stress-energy source. This can be partially addressed by working towards a limit in which increasingly smaller scales are resolved, and examining any scaling of nonlinear gravitational effects. We have also limited the dynamics allowed on large scales by imposing periodic boundary conditions. For a sufficiently large volume, or for a volume larger than our observable Universe, the boundary conditions are less relevant. The challenge then is resolving both of these scales simultaneously in a fully relativistic setting.

Lastly, we note that due to particle noise and the general expense of N-body calculations, it can be difficult to obtain reliable results using N-body simulations. The approach we use here takes advantage of recent developments in order to improve both performance and numerical convergence; however, cosmological simulations in general may stand to greatly benefit from the development of methods that converge at higher order, which can result in a lower computational cost per accuracy goal.

The agreement we find with linear theory in Newtonian and harmonic gauges is encouraging for standard cosmological theory in the context of the late universe. Yet, we also find that spacetimes may not always be well described by linear theory when sufficiently large overdensities or voids are present in these gauges. The inability of linear theory to accurately describe the synchronous gauge metric, on the other hand, implies that a fully relativistic treatment may generally be necessary to obtain the metric in that gauge. The large amplitude of nonlinear terms can, for example, explain the gravitational slip we observed in [9]; the amplitude of the slip was $\mathcal{O}(\mathcal{V})$, but it was computed by evaluating quantities from linear theory using the fully relativistic synchronous gauge metric, and was therefore found to be large. Nevertheless, additional linear-order gravitational corrections are still often neglected in literature, as in the approximate expression used in that work.

In this work we have shown the importance of considering linear theory in the context of a fully relativistic treatment. We have verified in a fully relativistic setting that

nonlinear corrections are of the expected magnitude for perturbations with amplitudes expected in a concordance cosmological model in Newtonian and harmonic gauge, and have explicitly demonstrated that large metric perturbations can be found in the presence of large density contrasts in synchronous gauge. We have also found that nonlinear effects can give rise to larger-than-expected metric perturbations when considering the most extreme structures in our Universe, approaching percent-level corrections to the metric even in Newtonian and harmonic gauges. These results suggest care should be taken when attempting to infer properties of the fully relativistic metric, and in the presence of extreme structures where linear theory may begin to fail.

ACKNOWLEDGMENTS

We would like to thank Matt Johnson, Will East, and Thomas Baumgarte for discussions that helped shape this work. This work benefited from the Sexten Center for Astrophysics workshop on GR effects in cosmological large-scale structure. This work made use of the High Performance Computing Resource in the Core Facility for Advanced Research Computing at Case Western Reserve University, as well as hardware provided by the National Science Foundation and the Kenyon College Department of Physics at Kenyon College. This research was supported in part by Perimeter Institute for Theoretical Physics. Research at Perimeter Institute is supported by the Government of Canada through the Department of Innovation, Science and Economic Development, Canada and by the Province of Ontario through the Ministry of Research, Innovation and Science. J. T. G. is supported by the National Science Foundation Grant No. PHY-1719652. J. B. M. acknowledges support as a CITA National Fellow. G. D. S. and C. T. were supported in part by Grant No. DE-SC0009946 from the US DOE.

APPENDIX A: A TOY DESCRIPTION OF CAUSTICS

Formally, the density will become infinite when the Jacobian $|\partial\vec{x}/\partial\vec{s}|$ is zero, a phenomenon that occurs during shell crossings. This is well known in Newtonian theory [62], but general relativistic studies of such phenomena are few, typically found in studies of relativistic collapse [28,30].

In the presence of an infinite density source, the full, general relativistic constraint equations imply that curvature scalars should also diverge. Because this can indicate the presence of a physical singularity, we would like to obtain solutions to the constraint equations to gain insight into the behavior of the metric in the vicinity of a caustic. To this end, we first consider a toy caustic in a universe with planar symmetry. We choose displacements

$$x(s) = s^{1+p} \tag{A1}$$

with p a positive integer (setting the dominant term in a series expansion around a caustic) so that for a constant ρ_s,

$$\sqrt{\gamma}\rho = \rho_s \left|\frac{\partial x}{\partial s}\right|^{-1} = \frac{\rho_s}{1+p}|x|^{-p/(1+p)}, \tag{A2}$$

which diverges when $s = 0$, or $x = 0$, and the severity of the divergence is controlled by p. Using the constraint equations and choosing an asymptotically flat and (3-) conformally flat spacetime with $K = 0$, or neglecting cosmological effects on the dynamics, the Hamiltonian constraint equation can be written in terms of the $3+1$ conformal factor ψ (where $\gamma^{1/2} = \psi^6$), and obeys

$$\nabla^2\psi = -2\pi\psi^5\rho. \tag{A3}$$

In the vicinity of the caustic, we can expand ψ in a power series for small x and find a solution that scales as

$$\psi \simeq 1 - 2\pi\rho_s \frac{2+p}{1+p}|x|^{\frac{2+p}{1+p}} \tag{A4}$$

and therefore does not diverge. The first derivative of ψ will also not diverge, indicating geodesics can be integrated through caustics without issue, although second derivatives, and therefore curvature scalars, may diverge. The mass present within a test region around the caustic also vanishes as the volume of the test region is decreased, indicating there is infinitesimal mass at the point of infinite density. Similar behavior may be found for a zero-dimensional caustic (i.e., radially displaced phase-space distribution).

For this toy solution, because the divergence of curvature scalars does not require the metric itself to diverge, the metric can remain in a weak-field limit. Because it is also possible to integrate geodesics through these caustics, such solutions do not appear to represent a singularity in the sense of a black hole.

Although this is a dimensionally reduced example, we do not empirically find caustics to lead to numerical instabilities or otherwise prevent us from performing our numerical integration (except in comoving-synchronous gauge/geodesic slicing). The primary drawback we encounter is a divergent computed Hamiltonian constraint violation due to subtracting numerically large values. In a standard Newtonian N-body setting, this difficulty is absent as the linearized constraint equations are directly used to determine the metric, so the dynamical Einstein equations are not enforced. In our case where both the metric and matter are dynamically evolved, we instead check for convergence of field profiles, and increased localization of the region in which a large GR constraint violation is observed.

APPENDIX B: A RELATIVISTIC GENERALIZATION OF NEWTONIAN GAUGE

As noted in the text, no true generalization of Newtonian gauge exists in a fully relativistic setting due to the presence

of additional degrees of freedom. In a planar-symmetric setting as studied here, general relativity can be directly mapped to Newtonian gravity for a judicious gauge choice [63], however this idea does not generalize to an asymmetric $3+1$ case, and thus we seek a more general condition. Perhaps the most commonly used generalization of Newtonian gauge is a "zero-shear" condition requiring

$$K^{ij}_{\rm TF} = 0, \tag{B1}$$

although other approaches to map results from Newtonian theory to a relativistic setting do exist [61]. In a linear setting this condition can be reduced to constraints on the scalar and vector modes. For the scalar modes in the absence of anisotropic stress, we can compare the Newtonian-gauge line element to the BSSN one as in the text below Eq. (20), and combine with one of the BSSN equations to produce a gauge condition,

$$\dot{\alpha} = \dot{\Phi}_N = -2\dot{\phi} = \frac{1}{3}\alpha K. \tag{B2}$$

While this resembles the harmonic gauge condition, it differs by an important minus sign that results in rapid growth of numerical error. Due to this growth, we therefore utilize Z4c constraint damping in order to stably evolve the system.

This choice also will not enforce the zero-shear condition beyond linear order. A generalization suggested by Bardeen [16] is to instead use a minimal-shear condition, such that

$$D_i D_j K^{ij}_{\rm TF} = 0. \tag{B3}$$

This choice reduces to Newtonian gauge in the scalar sector in the linear limit, and results in a 4th-order differential equation for α. However as solving an elliptic partial differential equation at every time step is computationally demanding, and anyway we wish to set initial conditions consistent with the synchronous gauge ones, we can instead seek a driver condition and look for a lapse such that the time-evolution equation for $K^{ij}_{\rm TF}$ is damped and not sourced at linear order. Damping of anisotropic stress is already present to an extent: the equations of motion

$$\begin{aligned}\partial_t K^{\rm TF}_{ij} &= \partial_t\left(K_{ij} - \frac{1}{3}\gamma_{ij}K\right)\\ &= \alpha R^{\rm TF}_{ij} - (D_iD_j\alpha)^{\rm TF} + \frac{1}{3}\alpha K K^{\rm TF}_{ij} - 2\alpha K^{\rm TF}_{ik}K^{k\rm TF}_{j}\\ &\quad - 8\pi\alpha S^{\rm TF}_{ij} + \beta^k\partial_k K_{ij} + K_{ik}\partial_j\beta^k + K_{jk}\partial_i\beta^k\\ &\quad - \frac{1}{3}\gamma_{ij}\beta^i D_i K - \frac{1}{3}(D_i\beta_j + D_j\beta_i)K\end{aligned} \tag{B4}$$

contain a damping term,

$$\partial_t K^{ij}_{\rm TF} \supset \frac{1}{3}\alpha K K^{\rm TF}_{ij}, \tag{B5}$$

along with dominant "source" terms

$$\partial_t K^{ij}_{\rm TF} \supset \alpha R^{\rm TF}_{ij} - (D_iD_j\alpha)^{\rm TF} + \text{shift}, \tag{B6}$$

where the "shift" denotes the contribution from the last line of Eq. (B4), which we will discuss later. In order to eliminate the first-order terms, we can attempt to choose a gauge for which

$$\alpha R^{\rm TF}_{ij} - (D_iD_j\alpha)^{\rm TF} = 0, \tag{B7}$$

as any existing $K^{ij}_{\rm TF}$ will naturally decay. As with the zero-shear condition, this condition cannot be fully satisfied, but can be minimized by solving

$$D^iD^j(\alpha R^{\rm TF}_{ij} - (D_iD_j\alpha)^{\rm TF}) = 0. \tag{B8}$$

This gauge condition again results in a 4th-order elliptic condition for α. It can be cast into a driver form by using the right-hand side as an evolution equation for the lapse,

$$\partial_t\alpha = \eta D^iD^j(\alpha R^{\rm TF}_{ij} - (D_iD_j\alpha)^{\rm TF}) \tag{B9}$$

for a driver strength coefficient η. An ordinary Laplacian D^2 acts as a viscous term, driving field values at a point to the local average value, resulting in standard diffusive behavior. The squared Laplacian D^2D^2 can be viewed in a similar way, but now with an additional frequency-dependent strength, and with the opposite sign. This minimal-shear condition can therefore be viewed as a diffusion equation, driving the field profile of α towards one that satisfies Eq. (B8).

Superluminal propagation may exist for this condition, depending on the driver coefficient and simulation resolution, imposing a strong restriction on the coefficient amplitude or quite small time step so that the Courant condition is satisfied. A future task would be to construct a condition absent of this requirement. Such a gauge would provide a generalization of Newtonian gauge that is well suited to numerical evolution, requiring neither an especially small time step nor require solving an elliptic equation at each time step. This idea has been explored in a Newtonian setting [64], and the superior scaling properties demonstrated in that context. Mapping a general relativistic gauge condition to the hyperbolic equations of motion found in [64] would provide a means of interpreting these results in a relativistic context without requiring a large speed of propagation of gravity.

In order partially to alleviate this problem, we both linearize and act the inverse Laplacian on the right-hand side of (B9) in order to cast it into a more standard diffusive

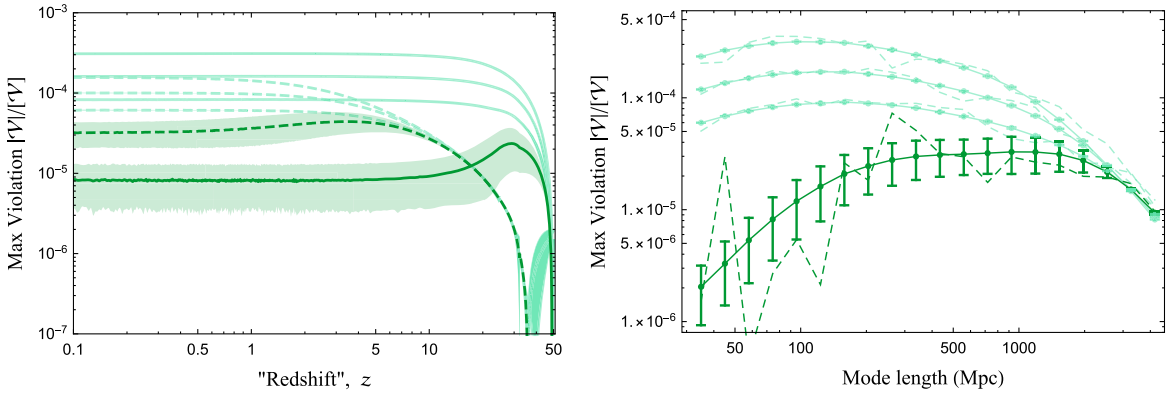

FIG. 4. Similar to Figs. 1 and 2, we show the relative violation of the linearized Einstein equations, both as a function of mode and FLRW redshift. Light (top three) lines indicate Newtonian results with different values of the driver coefficient ($\eta_G = 0.005, 0.01, 0.02$ top to bottom), and dark green the extrapolated $\eta_G \to \infty$ limit as described in the text. The left plot shows the violation as a function of redshift, and the right plot shows the violation "today" (redshift zero). Other parameters are as in Figs. 1 and 2.

form, for which α will still be driven towards the desired value,

$$\partial_t \alpha = \eta_G \left(\frac{2}{3} \nabla^2 \alpha - \frac{1}{\nabla^2} \sum_{i,j} \partial_i \partial_j R^{\mathrm{TF}}_{ij} \right), \tag{B10}$$

although we still need to compute an inverse Laplacian. We unsurprisingly find that this gauge is not stable numerically, but the use of Z4c constraint damping still allows solutions to be found. However, even after acting the inverse Laplacian, the time step required for stability is still quite small. We nevertheless find this driver condition to perform better than the choice of Eq. (B9), or acting the inverse Laplacian twice (which results in another unstable gauge condition for which the behavior resembles exponential decay instead of diffusion).

It is also possible to minimize the vector contribution to K_{ij} by setting the linearized vector contribution to zero. In cosmology, this choice together with the linearized minimal-shear lapse condition comprises longitudinal or Poisson gauge. A nonlinear generalization of this shift condition is the minimal distortion shift [43]. A conformally related, somewhat simplified choice for the shift is widely employed in numerical relativity simulations in a hyperbolic driver form, with

$$\begin{aligned} \partial_t \beta^i &= k B^i \\ \partial_t B^i &= \partial_t \bar{\Gamma}^i - \eta_B B^i, \end{aligned} \tag{B11}$$

commonly known as the "gamma-driver" condition [65,66]. In the limit $k \to \infty$ and $\eta_B \to \infty$, and in a linearized setting, the longitudinal/Poisson gauge condition should be recovered.

Although the utility of the gamma-driver gauge condition has been demonstrated throughout numerical relativity literature, we do not use this shift condition in the simulations in this work. The gauge choice of $\beta^i = 0$ that we employ results in vector modes instead residing in the 3-metric; these modes should decay on the scales we consider [15].

The final results we obtain in the Newtonian driver gauge are sensitive to the diffusion coefficient in the gauge, with larger coefficients generally found to result in a smaller amount of linearized constraint violation. In order to provide a measure for the linearized constraint violation in the limit that the diffusion coefficient is infinite, we note that we see the difference between measured linearized violations follow a power law,

$$\frac{\mathcal{V}}{[\mathcal{V}]} \simeq \left. \frac{\mathcal{V}}{[\mathcal{V}]} \right|_{\eta_G = \infty} + \frac{A}{\eta_G^p}, \tag{B12}$$

with $p \sim 1$ determined empirically. We can then take the limit that $\eta_G \to \infty$ in a manner similar to Richardson extrapolation. Unfortunately this exponent does not work perfectly in all cases: the exponent inferred from the observed convergence rate varies by tens of percent, leading to appreciable error bars in the final, extrapolated values. The extrapolated values nevertheless agree to within the error bars for different choices of p within this range, so we expect our results including error bars to robustly quantify the correct order of magnitude of violation of linear theory in the $\eta_G \to \infty$ limit. Results for several choices of η_G can be seen in Fig. 4, along with the mean violation extrapolated using all pairs of runs, and error inferred from the standard deviation of this distribution.

APPENDIX C: NUMERICAL CONVERGENCE

We briefly describe numerical convergence of our results, focusing on the results from Sec. III B in harmonic gauge, which make use of the particle code and can be run at high resolutions for comparisons. As noted in the text,

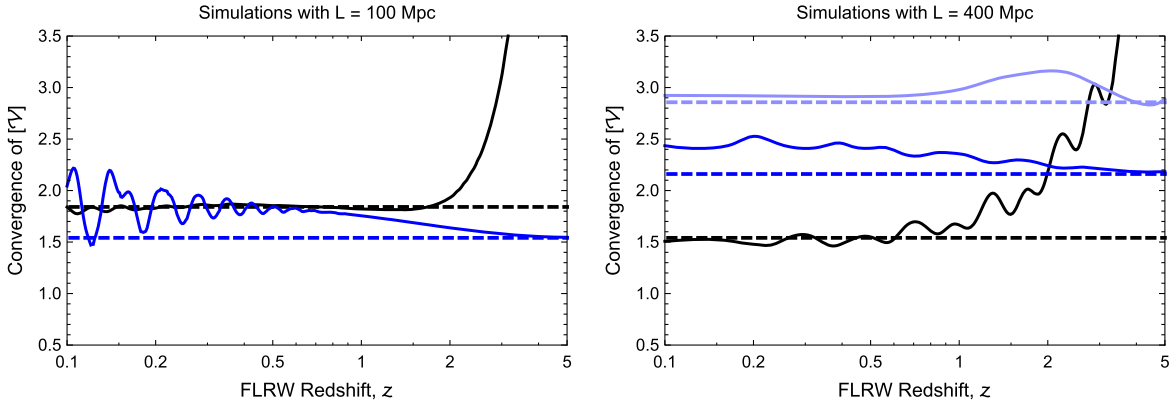

FIG. 5. Numerical convergence of the violation magnitude $[\mathcal{V}]$. Dashed lines indicate theoretical 2nd-order convergence, and solid lines computed convergence. Black lines indicate 3D/asymmetric runs, and dark blue lines 1D/planar-symmetric runs. Light blue lines indicate results from planar-symmetric Newtonian gauge runs with $\eta_G = 0.02$, while all other runs used harmonic slicing. Resolutions are as described in the text of Sec. III B.

we generally find runs converge at second order in the grid resolution Δx. For sufficiently large time steps, 4th-order error from RK4 time stepping can dominate: larger physical box sizes allow larger physical time steps taken due to the Courant condition. Error from the 8th-order finite differencing scheme we use was not usually the dominant error source for the runs we present in this paper, although may in some cases depending upon choices of numerical parameters. In order for simulations to numerically converge, the number of particles per smoothing volume—per configuration-space grid cell in our case—must also tend towards infinity [67]. Without imposing this condition when noise dominates the error, we can find nonconvergent and inaccurate field values. Along with the Courant condition, increasing particle number per grid cell in order to reduce noise poorly impacted scaling in a higher-dimensional setting.

In Fig. 5, we show the convergence rate of the violation magnitude $[\mathcal{V}]$ with resolution,

$$\mathcal{C} = \frac{[\mathcal{V}]_{\Delta x_1} - [\mathcal{V}]_{\Delta x_2}}{[\mathcal{V}]_{\Delta x_2} - [\mathcal{V}]_{\Delta x_3}}, \tag{C1}$$

for runs with various resolutions $\Delta x_1 > \Delta x_2 > \Delta x_3$. Parameters of these runs are as presented in Sec. III B. In all cases, the convergence rate is found to be second order in Δx. Although not shown explicitly, similar convergence is found for other fields.

For the perfect fluid evolved in synchronous gauge, we find convergence in agreement with the 8th-order finite difference method used for sufficiently small time steps, and 4th-order convergence in the case that error due to time stepping is dominant. Synchronous gauge results are also Richardson extrapolated assuming appropriate convergence.

The error bars or "confidence intervals" we report come from the distributions of extrapolated values. We typically run at three resolutions and can therefore produce three extrapolated values using three unique pairs or runs, and one extrapolation using all three runs. The extrapolated values typically agree well, except in the case of zero crossings of $\mathcal{V}$ or $\mathcal{K}$. In these cases, uncertainty is dominated by uncertainty in the precise time of the zero crossing, which in turn is highly sensitive to truncation error. However, in these cases, the computed violations were also found to be uninterestingly physically small.

[1] C. C. Dyer and R. C. Roeder, Gen. Relativ. Gravit. **13**, 1157 (1981).
[2] P. Fleury, J. Larena, and J.-P. Uzan, Phys. Rev. Lett. **119**, 191101 (2017).
[3] T. Clifton, K. Rosquist, and R. Tavakol, Phys. Rev. D **86**, 043506 (2012).
[4] M. Korzyński, Classical Quantum Gravity **32**, 215013 (2015).
[5] V. Tansella, C. Bonvin, R. Durrer, B. Ghosh, and E. Sellentin, J. Cosmol. Astropart. Phys. 03 (2018) 019.
[6] O. Umeh, S. Jolicoeur, R. Maartens, and C. Clarkson, J. Cosmol. Astropart. Phys. 03 (2017) 034.
[7] P. Fleury, C. Clarkson, and R. Maartens, J. Cosmol. Astropart. Phys. 03 (2017) 062.
[8] W. E. East, R. Wojtak, and T. Abel, Phys. Rev. D **97**, 043509 (2018).

[9] J. T. Giblin, J. B. Mertens, G. D. Starkman, and A. R. Zentner, Phys. Rev. D **96**, 103530 (2017).
[10] E. Bentivegna and M. Bruni, Phys. Rev. Lett. **116**, 251302 (2016).
[11] J. T. Giblin, J. B. Mertens, and G. D. Starkman, Astrophys. J. **833**, 247 (2016).
[12] J. T. Giblin, J. B. Mertens, and G. D. Starkman, Phys. Rev. Lett. **116**, 251301 (2016).
[13] H. Macpherson, D. J. Price, and P. D. Lasky, arXiv:1807.01711.
[14] H. J. Macpherson, P. D. Lasky, and D. J. Price, Astrophys. J. **865**, L4 (2018).
[15] S. Weinberg, Cosmology, ISBN: 9780198526827, http://www.oup.com/uk/catalogue/?ci=9780198526827.
[16] J. M. Bardeen, Phys. Rev. D **22**, 1882 (1980).
[17] S. R. Green and R. M. Wald, Classical Quantum Gravity **31**, 234003 (2014).
[18] J. Adamek, C. Clarkson, D. Daverio, R. Durrer, and M. Kunz, Classical Quantum Gravity **36**, 014001 (2019).
[19] T. Nakamura, K. Oohara, and Y. Kojima, Prog. Theor. Phys. Suppl. **90**, 1 (1987).
[20] M. Shibata and T. Nakamura, Phys. Rev. D **52**, 5428 (1995).
[21] T. W. Baumgarte and S. L. Shapiro, Phys. Rev. D **59**, 024007 (1998).
[22] J. B. Mertens, J. T. Giblin, and G. D. Starkman, Phys. Rev. D **93**, 124059 (2016).
[23] J. T. Giblin, J. B. Mertens, and G. D. Starkman, Classical Quantum Gravity **34**, 214001 (2017).
[24] T. W. Baumgarte and S. L. Shapiro, *Numerical Relativity: Solving Einstein's Equations on the Computer* (Cambridge University Press, Cambridge, England, 2010).
[25] M. Alcubierre, *Introduction to 3+1 Numerical Relativity*, International Series of Monographs on Physics (Oxford University Press, Oxford, 2008).
[26] S. Bernuzzi and D. Hilditch, Phys. Rev. D **81**, 084003 (2010).
[27] Z. Cao and D. Hilditch, Phys. Rev. D **85**, 124032 (2012).
[28] C.-M. Yoo, T. Harada, and H. Okawa, Classical Quantum Gravity **34**, 105010 (2017).
[29] L. Lehner, Classical Quantum Gravity **18**, R25 (2001).
[30] S. L. Shapiro and S. A. Teukolsky, Astrophys. J. **298**, 34 (1985).
[31] M. Shibata, Prog. Theor. Phys. **101**, 251 (1999).
[32] M. Shibata, Prog. Theor. Phys. **101**, 1199 (1999).
[33] F. Pretorius and W. E. East, Phys. Rev. D **98**, 084053 (2018).
[34] H. J. Macpherson, P. D. Lasky, and D. J. Price, Phys. Rev. D **95**, 064028 (2017).
[35] E. Bentivegna, Phys. Rev. D **95**, 044046 (2017).
[36] E. Bentivegna, T. Clifton, J. Durk, M. Korzyński, and K. Rosquist, Classical Quantum Gravity **35**, 175004 (2018).
[37] J. Adamek, D. Daverio, R. Durrer, and M. Kunz, Nat. Phys. **12**, 346 (2016).
[38] J. Feng, M. Baumann, B. Hall, J. Doss, L. Spencer, and R. Matzner, Astrophys. J. **859**, 130 (2018).
[39] O. Hahn and R. E. Angulo, Mon. Not. R. Astron. Soc. **455**, 1115 (2016).
[40] T. Abel, O. Hahn, and R. Kaehler, Mon. Not. R. Astron. Soc. **427**, 61 (2012).
[41] Ya. B. Zeldovich, Astron. Astrophys. **5**, 84 (1970).
[42] M. T. Gastner and M. E. J. Newman, Proc. Natl. Acad. Sci. U.S.A. **101**, 7499 (2004).
[43] L. Smarr and J. W. York, Jr, Phys. Rev. D **17**, 2529 (1978).
[44] C.-M. Yoo, H. Okawa, and K.-i. Nakao, Phys. Rev. Lett. **111**, 161102 (2013).
[45] V. F. Mukhanov, H. A. Feldman, and R. H. Brandenberger, Phys. Rep. **215**, 203 (1992).
[46] E. Bertschinger, arXiv:astro-ph/9503125.
[47] J. Adamek, J. Brandbyge, C. Fidler, S. Hannestad, C. Rampf, and T. Tram, Mon. Not. R. Astron. Soc. **470**, 303 (2017).
[48] J. Adamek, R. Durrer, and M. Kunz, J. Cosmol. Astropart. Phys. 11 (2017) 004.
[49] S. F. Daniel, R. R. Caldwell, A. Cooray, and A. Melchiorri, Phys. Rev. D **77**, 103513 (2008).
[50] D. Jeong and F. Schmidt, Phys. Rev. D **89**, 043519 (2014).
[51] A. Lewis and S. Bridle, Phys. Rev. D **66**, 103511 (2002).
[52] E. Bentivegna, Springer Proc. Math. Stat. **60**, 143 (2014).
[53] E. Bentivegna and M. Korzynski, Classical Quantum Gravity **30**, 235008 (2013).
[54] C.-M. Yoo and H. Okawa, Phys. Rev. D **89**, 123502 (2014).
[55] E. Bentivegna, M. Korzyński, I. Hinder, and D. Gerlicher, J. Cosmol. Astropart. Phys. 03 (2017) 014.
[56] S. R. Goldberg, T. Clifton, and K. A. Malik, Phys. Rev. D **95**, 043503 (2017).
[57] R. K. Sheth and A. Diaferio, Mon. Not. R. Astron. Soc. **417**, 2938 (2011).
[58] R. C. Keenan, A. J. Barger, and L. L. Cowie, Astrophys. J. **775**, 62 (2013).
[59] I. Szapudi *et al.*, Mon. Not. R. Astron. Soc. **450**, 288 (2015).
[60] S. Jolicoeur, O. Umeh, R. Maartens, and C. Clarkson, J. Cosmol. Astropart. Phys. 03 (2018) 036.
[61] C. Fidler, T. Tram, C. Rampf, R. Crittenden, K. Koyama, and D. Wands, J. Cosmol. Astropart. Phys. 12 (2017) 022.
[62] V. I. Arnold, S. F. Shandarin, and I. B. Zeldovich, Geophys. Astrophys. Fluid Dyn. **20**, 111 (1982).
[63] R. B. Mann (1989).
[64] R. Hirai, H. Nagakura, H. Okawa, and K. Fujisawa, Phys. Rev. D **93**, 083006 (2016).
[65] M. Alcubierre and B. Brugmann, Phys. Rev. D **63**, 104006 (2001).
[66] M. D. Duez, P. Marronetti, S. L. Shapiro, and T. W. Baumgarte, Phys. Rev. D **67**, 024004 (2003).
[67] Q. Zhu, L. Hernquist, and Y. Li, Astrophys. J. **800**, 6 (2015).